



**HAL**  
open science

# Physical limits to human brain B0 shimming, engineering implications thereof

Bruno Pinho Meneses, Alexis Amadon

► **To cite this version:**

Bruno Pinho Meneses, Alexis Amadon. Physical limits to human brain B0 shimming, engineering implications thereof. 2021. hal-03210241v2

**HAL Id: hal-03210241**

**<https://hal.science/hal-03210241v2>**

Preprint submitted on 6 Dec 2021

**HAL** is a multi-disciplinary open access archive for the deposit and dissemination of scientific research documents, whether they are published or not. The documents may come from teaching and research institutions in France or abroad, or from public or private research centers.

L'archive ouverte pluridisciplinaire **HAL**, est destinée au dépôt et à la diffusion de documents scientifiques de niveau recherche, publiés ou non, émanant des établissements d'enseignement et de recherche français ou étrangers, des laboratoires publics ou privés.

# Physical Limits to Human Brain B0 Shimming, Engineering Implications Thereof

Bruno Pinho Meneses and Alexis Amadon

Université Paris-Saclay, CEA, CNRS, BAOBAB, NeuroSpin,  
91191 Gif-sur-Yvette, France.

\*Corresponding author(s). E-mail(s): [alexis.amadon@cea.fr](mailto:alexis.amadon@cea.fr);

## Abstract

**Objective** As the MRI main magnetic field rises for improved Signal-to-Noise Ratio, susceptibility-induced B0-inhomogeneity increases proportionally, aggravating related artifacts. Considering only susceptibility disparities between air and biological tissue, we explore the topological conditions for which perfect shimming could be performed in a Region of Interest (ROI) such as the human brain or part thereof. **Materials and Methods** After theoretical considerations for perfect shimming, spherical harmonic (SH) shimming simulations of very high degree are performed, based on a 100-subject database of 1.7-mm-resolved brain fieldmaps acquired at 3 T. In addition to the whole brain, shimmed ROIs include slabs targeting the prefrontal cortex, both or single temporal lobes, or spheres in the frontal brain above the nasal sinus. **Results and Discussion** We show “perfect” shimming is possible only if the ROI can be contained in a sphere that does not enclose sources of magnetic field inhomogeneity, which are gathered at the air-tissue interface. We establish a 12 Hz inhomogeneity hard shim limit at 7 T for whole brain shimming, that can only be attained at shimming degree higher than 90. On the other hand, under limited power and SH degree resources, 3D region-specific shimming is shown to greatly improve homogeneity in critical zones such as the prefrontal cortex and around ear canals.

# 1 Introduction

When immersed in the uniform magnetic field  $B_0$  of the MRI scanner, the media composing the human head (biological tissue, air) become magnetized, in turn generating a non-uniform magnetic field distribution  $\delta B_0(\mathbf{x})$  obeying:

$$\nabla^2 \delta B_0 = \left( \nabla^2 \chi - 3 \frac{\partial^2 \chi}{\partial z^2} \right) \frac{B_0}{3}, \quad (1)$$

(adapted from equation 14 of Salomir *et al.* 2003 [1]) where  $\chi(\mathbf{x})$  is the media's magnetic susceptibility.

Such inhomogeneous magnetic field distribution is at the origin of several kinds of image artifacts in human brain imaging, with geometric distortion in Echo Planar acquisitions being a notorious example [2–7].

As an example, in non-accelerated Echo-Planar Imaging (EPI) single-shot acquisitions, under 0.5 ms inter-echo spacing and 200 mm Field-of-View (FOV) in the phase encoding direction, a 100 Hz excursion in the magnetic field leads to 10 mm geometric distortion in the reconstructed image [3–5]. It is therefore not surprising that appreciable effort has been directed to the design of shimming systems for the human brain [8–15], but as we will see, they are still far from achieving the minimal inhomogeneity.

Other  $B_0$  related complications are signal loss in  $T_2^*$ -weighted imaging [5], banding artefacts in Steady-State Free Precession sequences [11], failed inversion-recovery pulse, inhomogeneous flip angle distribution [16], and line broadening in spectroscopy [17].

With the current trend of increasing magnetic field intensity of clinical and research MRI scanners (7 T Siemens Terra, 10.5 T at the Center for Magnetic Resonance Research (CMRR) [18], 11.7 T Iseult project [19]) to achieve

higher SNR and Contrast-to-Noise Ratio (CNR), susceptibility-induced inhomogeneity rises proportionally to the main field. High performance static field shimming becomes crucial for these scanners to deliver their full potential in applications such as functional MRI (fMRI) [20].

Correction of inhomogeneous fields is either active, generated by electric current flow in conductors located around the patient, or passive, by the placement of ferromagnetic pieces in optimal positions [21–23]. This subject specific shimming is performed in clinical routine by Spherical Harmonics (SH) based systems integrated to the MRI scanner, commonly of 2<sup>nd</sup> degree and eventually up to 3<sup>rd</sup> degree. To improve shimming performances, higher-degree SH-based systems have also been employed [24], containing up to partial 5<sup>th</sup> degree. Moreover, non-SH-based Multi-Coil Array (MCA) systems [8, 9, 25, 26] have gained traction in the last years. These have been shown to provide adequate homogeneity for numerous applications at Ultra High Field (UHF), particularly in dynamic shimming mode [8, 10], but strong field excursions persist around the ear canals and in the pre-frontal cortex despite shimming, even when employing brain-optimized MCAs [11–15, 27–29].

Aware of these unmet needs, we first analyze and demonstrate why perfect shimming of an entire human brain is impossible, based on theory and topological considerations. Then we explore the limits of  $B_0$  shimming through unconstrained SH shimming simulations on a large database of brain 3D fieldmaps. Furthermore, assessment of realistic shim systems is performed through power constrained coil design, where homogeneity levels attained by such systems will be compared to the lowest achievable homogeneity. Knowledge of the attainable levels of homogeneity for diverse shimming strategies (whole-brain, region-specific, slice-wise) can provide meaningful insight for future shim system design, since for limited resources (channel count,

maximum current and power), a region-specific shimming strategy could provide homogeneity levels unattainable when applying global (whole-brain) shimming.

## 2 Theory: Physical Limits to B0 Shimming

Although there are mentions in the literature to the impossibility of perfectly shimming the magnetic field inside the brain [30], no detailed account on the reason for such limitation has been provided. Here we will show that, even if the brain could be considered as a source-free homogeneous medium, air-induced dipole sources located outside the brain, but within concave regions thereof, cannot be overcome.

### 2.1 Mathematical Analysis of Magnetic Field Sources Around the Brain

$B_0$  homogeneity in the human brain is mainly disturbed by the presence of susceptibility gradients, according to equation 1. The magnetic field source distribution can be computed in every voxel from the right side of that equation:

$$\rho_m(\mathbf{x}) = \left( \nabla^2 \chi - 3 \frac{\partial^2 \chi}{\partial z^2} \right) \frac{B_0}{3}. \quad (2)$$

In the human head, susceptibility gradients are dominant between paramagnetic air cavities and diamagnetic tissues. Susceptibility differences within the brain also exist between white matter, gray matter and cerebrospinal fluid, but are less significant in comparison to that between air and tissues. Indeed, the brain magnetic susceptibility variations caused by iron or myelin content lie in a 0.4 ppm range [31]. On the other hand, 2<sup>nd</sup>-order poorly-corrected air-induced inhomogeneities extend an order-of-magnitude above this range, as

can actually be observed from B<sub>0</sub> brain maps (see B<sub>0</sub>-map examples in Methods). Therefore here we suppose tissue susceptibility disparities are negligible compared to air-induced inhomogeneities. This assumption is convenient since air-induced inhomogeneities are precisely what we want to correct. Provided this assumption holds, we are left with homogeneous source-free brain tissue. In that context, Laplace’s equation applies in the brain (cf. next section).

Localized susceptibility gradients at the interface between air and tissue act as a distribution of infinitesimal magnetic dipoles. Indeed if we apply equation 2 to a susceptibility map with two homogeneous media (one diamagnetic, the other one paramagnetic) separated by an interface, the finite difference method will lead to a high value on one side of the boundary, and an equal intensity but opposite sign value right at the other side of the boundary. We end up with a positive monopole on one side, a negative monopole on the other side, very close to each other, which constitute the dipole on the boundary. For the human head, a surface distribution of dipole moments disturbing the once uniform magnetic field appears, located around the ear canals, sinus, mouth and any other air-tissue interface.

An infinitesimal magnetic dipole can be considered as a fundamental building-block to analyze the sample-induced B<sub>0</sub> inhomogeneity, defined as the B<sub>0</sub> standard deviation to mean ratio across the Region-Of-Interest (ROI).

To counteract the inhomogeneous magnetic field, active shimming systems are commonly employed, and an infinitesimal current filament can be used as another fundamental building block to describe the magnetic field of such systems.

Both fundamental pieces are depicted in Fig. 1. The perturbation is produced by a magnetic dipole of moment  $\mathbf{m}_p = m_p \hat{\mathbf{z}}$ , located at some arbitrary location  $\mathbf{x}_p$  with spherical coordinates  $(r_p, \theta_p, \varphi_p)$ ; and the correction field is

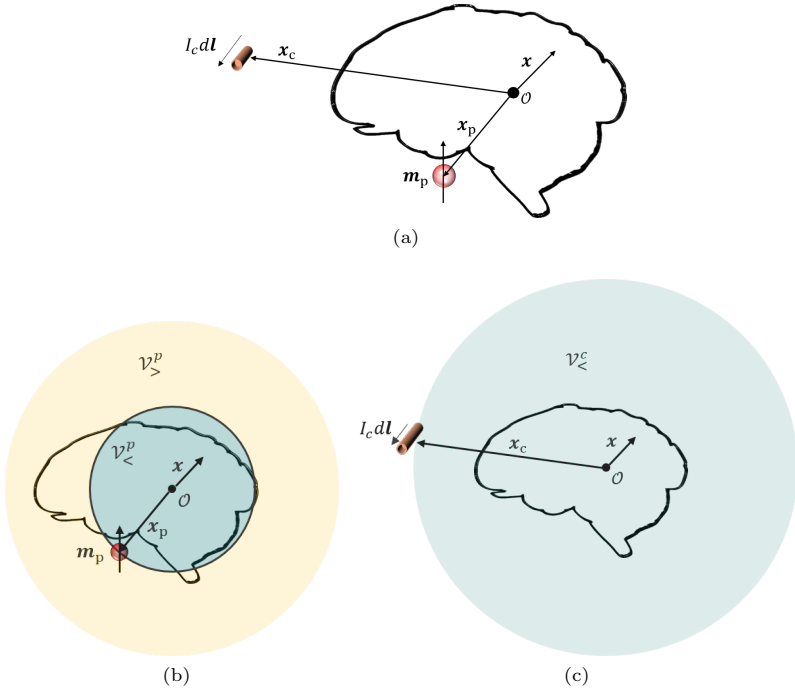


**Fig. 1:** (a) Disposition of fundamental building blocks for sample-induced magnetic field perturbation ( $\mathbf{m}_p$ ) and field correction ( $I_c dl$ ) around the brain. The MR magnet isocenter at  $\mathcal{O}$  corresponds to the origin of the  $B_0$  SH-decomposition. Vector  $\mathbf{x} \in \mathbb{R}^3$  points to an arbitrary brain voxel to be shimmed. (b) A representation of the regions where the magnetic field generated by a punctual sample-induced perturbation is described by RSH ( $\mathcal{V}_{<}^p$ ) and ISH ( $\mathcal{V}_{>}^p$ ). (c) The region  $\mathcal{V}_{<}^c$  where the correction magnetic field is decomposed into RSH.

produced by a wire filament carrying current  $I_c$ , with length  $dl$ , located at  $\mathbf{x}_c$  with spherical coordinates  $(r_c, \theta_c, \varphi_c)$  relative to SH isocenter  $\mathcal{O}$ .

## 2.2 Laplace's Equation and Solid Harmonics

Any magnetic field in a source-free region such as the presumably homogeneous human brain obeys Laplace's equation. In the subsequent analysis, the reference coordinate frame is defined such that the main  $B_0$  field is oriented

in the positive  $z$  direction. In the  $z$  direction, the Laplace equation is written:

$$\nabla^2 B_z(r, \theta, \varphi) = 0. \quad (3)$$

This equation has a general solution given by:

$$B_z(r, \theta, \varphi) = \sum_{n=0}^{+\infty} \sum_{m=-n}^n A_n^m \mathcal{R}_n^m(r, \theta, \varphi) + B_n^m \mathcal{I}_n^m(r, \theta, \varphi) \quad (4)$$

with

$$\mathcal{R}_n^m(r, \theta, \varphi) = r^n Y_n^m(\theta, \varphi), \quad (5)$$

$$\mathcal{I}_n^m(r, \theta, \varphi) = \frac{1}{r^{n+1}} Y_n^m(\theta, \varphi) \quad (6)$$

and

$$Y_n^m(\theta, \varphi) = \begin{cases} P_n^m(\cos \theta) \cos m\varphi & m \geq 0 \\ P_n^{|m|}(\cos \theta) \sin |m|\varphi & m < 0 \end{cases}, \quad (7)$$

where  $\mathcal{R}_n^m$ ,  $\mathcal{I}_n^m$  and  $Y_n^m$  are denominated Regular Solid Harmonic (RSH), Irregular Solid Harmonic (ISH) and Spherical (or Surface) Harmonic (SH), respectively, of degree  $n$  and order  $m$ ; and functions  $P_n^m : [-1, 1] \rightarrow \mathbb{R}$  are Associated Legendre Polynomials given by

$$P_n^m(x) = \frac{(1-x^2)^{\frac{m}{2}}}{2^n n!} \frac{d^{n+m}}{dx^{n+m}} (x^2-1)^n. \quad (8)$$

Examples of SH shapes are represented on a unit sphere in Fig. 2. Using the above definitions for RSH and ISH, the particular Green function for the Laplacian,  $1/|\mathbf{x} - \mathbf{x}'|$ , present in the formulas of scalar and vector magnetic potentials in magneto-statics, can be expanded into (adapted from Jackson [32]):



$$\frac{1}{|\mathbf{x} - \mathbf{x}'|} = \sum_{n=0}^{+\infty} \sum_{m=0}^n (2 - \delta_{m0}) \frac{(n-m)!}{(n+m)!} \frac{r_{<}^n}{r_{>}^{n+1}} P_n^m(\cos \theta) P_n^m(\cos \theta') \cos m(\varphi - \varphi') \quad (9)$$

with  $r_{>}$  ( $r_{<}$ ) the larger (smaller) between  $|\mathbf{x}|$  and  $|\mathbf{x}'|$ ; and  $\delta_{m0}$  the Kronecker delta.

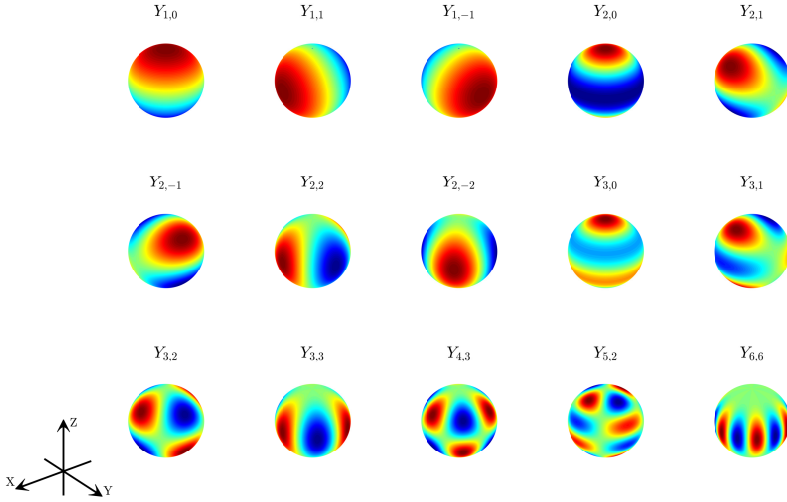


**Fig. 2:** Examples of Spherical Harmonic functions of various degrees and orders (cf. equation 7).

### 2.2.1 Solid Harmonic Expansion of Sample Induced Perturbation

To analyze the magnetic field generated by  $\mathbf{m}_p$  inside the brain, it is convenient to employ the magnetic scalar potential, given by:

$$\Phi_p(\mathbf{x}) = -\frac{\mathbf{m}_p}{4\pi} \cdot \nabla \frac{1}{|\mathbf{x} - \mathbf{x}_p|}. \quad (10)$$

From  $\mathbf{B} = -\mu_0 \nabla \Phi$ , the magnetic field in the  $z$  direction is

$$B_z^p(\mathbf{x}) = \frac{\mu_0 m_p}{4\pi} \frac{\partial^2}{\partial z^2} \frac{1}{|\mathbf{x} - \mathbf{x}_p|}. \quad (11)$$

Substituting eq. 9 into eq. 11, according to the position of the point of interest  $\mathbf{x}$  relatively to  $\mathbf{x}_p$ , one obtains two possible expressions for the magnetic field.

Those are:

$$B_z^p(\mathbf{x}) = \frac{\mu_0 m_p}{4\pi r_p^3} \sum_{n=0}^{+\infty} \sum_{m=0}^n (2 - \delta_{m0}) \frac{(n - m + 2)!}{(n + m)!} \frac{P_{n+2}^m(\cos \theta_p)}{r_p^n} r^n P_n^m(\cos \theta) \cos m(\varphi - \varphi_p), \quad (12)$$

in  $\mathcal{V}_<^p = \{\mathbf{x} \in \mathbb{R}^3 : |\mathbf{x}| < r_p\}$ , and

$$B_z^p(\mathbf{x}) = \frac{\mu_0 m_p}{4\pi} \sum_{n=2}^{+\infty} \sum_{m=0}^{n-2} \frac{(2 - \delta_{m0})(n - m)!}{(n + m - 2)!} P_{n-2}^m(\cos \theta_p) \frac{r_p^{n-2}}{r^{n+1}} P_n^m(\cos \theta) \cos m(\varphi - \varphi_p) \quad (13)$$

in  $\mathcal{V}_>^p = \{\mathbf{x} \in \mathbb{R}^3 : |\mathbf{x}| > r_p\}$ . Equation 12 was adapted from Romeo & Hoult, 1984 [21], and equation 13 can be derived in a similar fashion.

Therefore we notice that in  $\mathcal{V}_<^p$  the magnetic field is composed exclusively of RSH, while ISH describe the magnetic field in  $\mathcal{V}_>^p$ . Moreover, let  $\mathcal{V}_b$  be the brain region, the sample induced perturbations can produce both RSH and ISH fields in its interior as long as the intersection of  $\mathcal{V}_b$  with sets  $V_<^p$  and  $V_>^p$  is non-null.

### 2.2.2 Solid Harmonic Expansion of Correction Fields

With the inhomogeneous field described, we move our attention to the correction fields. The filament chosen as building-block for correction devices has

magnetic vector potential given by

$$d\mathbf{A}_c(\mathbf{x}) = \frac{\mu_0 I_c d\mathbf{l}}{4\pi} \frac{1}{|\mathbf{x} - \mathbf{x}_c|} \quad (14)$$

producing

$$dB_z^c(\mathbf{x}) = \hat{z} \cdot (\nabla \times d\mathbf{A}_c(\mathbf{x})) \quad (15)$$

as magnetic field in the  $z$  direction.

Substitution of eq. 9 into eq. 14 and subsequent calculation of eq. 15 leads to (adapted from Romeo & Hoult, 1984 [21]):

$$dB_z^c(r, \theta, \phi) = \frac{\mu_0 I_c \sin \theta_c d\varphi}{4\pi} \sum_{n=0}^{+\infty} \sum_{m=0}^{n+1} \left[ \frac{(n-m)!}{(n+m)!} \frac{P_{n+1}^{m+1}(\cos \theta_c)}{r_c^{n+1}} - \frac{(n-m+2)!}{(n+m)!} \frac{P_{n+1}^{m-1}(\cos \theta_c)}{r_c^{n+1}} \right] \times r^n P_n^m(\cos \theta) \cos m(\varphi - \varphi_c). \quad (16)$$

in  $\mathcal{V}_c^c = \{\mathbf{x} \in \mathbb{R}^3 : |\mathbf{x}| < r_c\}$ .

As the shimming system is positioned around the patient's body or head, we have  $\mathcal{V}_b \subset \mathcal{V}_c^c$ ; therefore, equation 16 is sufficient for describing the magnetic field in the subject's brain generated by shimming structures, and it is observed that this magnetic field only generates RSH.

### 2.2.3 Condition for Perfect B0 Shimming

RSH and ISH functions are linearly independent. Therefore, any shimming apparatus placed around the head can only zero-out the sample-induced inhomogeneity in the brain if  $\mathcal{V}_b^c \cap \mathcal{V}_b = \emptyset$ , i.e. there is no ISH term describing the magnetic field inside the brain. Or, stated in a simpler and generalized form, a region within an anatomy can only be shimmed to a perfectly homogeneous

magnetic field by an external shimming apparatus if, and only if, the smallest sphere enclosing said region does not contain any source of magnetic field.

### 3 Methods

We start by showing that the human brain does not satisfy the condition for perfect  $B_0$  homogenization. Then, by performing RSH shimming in a large database of  $\delta B_0$  fieldmaps, the minimal inhomogeneity theoretically achievable  $\sigma_{\min}$  is estimated. In addition, we discuss how state-of-the-art shimming systems compare to the best achievable inhomogeneity. Different regions of interest are explored in this phase to compare global, slice-by-slice and slab-specific shimming.

Finally, the estimated ultimate inhomogeneity is compared to what could be achieved by optimal shim coils under power constraints.

#### 3.1 Source Localization in a 3D Head Model

First we used a 3D model of the human head [33], with magnetic susceptibilities of air and tissues set to  $\chi_a = 0.36 \times 10^{-6}$  and  $\chi_t = -9.03 \times 10^{-6}$ , respectively. Once  $\rho_m$  is calculated from equation 2, the set  $\mathcal{X} = \{|\mathbf{x}| : \rho_m(\mathbf{x}) \neq 0\}$  can be defined. Let  $\mathcal{B}(\text{inf } \mathcal{X}, \mathcal{O})$  be a ball<sup>1</sup> of radius  $\text{inf } \mathcal{X}$ , centered at  $\mathcal{O}$ , according to our proposition, if  $\mathcal{B} \cap \mathcal{V}_b \neq \mathcal{V}_b$ , the brain cannot be perfectly shimmed by RSH. Nevertheless,  $\mathcal{B}(\text{inf } \mathcal{X}, \mathcal{O})$  or any other ball inside the brain (not necessarily centered at  $\mathcal{O}$ ), not enclosing magnetic field sources, could still be perfectly shimmed.

---

<sup>1</sup>A ball  $\mathcal{B}(R, \mathbf{c})$  of radius  $R$  centered at  $\mathbf{c} \in \mathbb{R}^3$  is defined as the set of  $\mathbf{x} \in \mathbb{R}^3$  such that  $|\mathbf{x} - \mathbf{c}| < R$ .

## 3.2 Acquisition of a large reference brain field-map database

To determine the best achievable homogeneity under the theoretical limits, unconstrained RSH shimming simulations with increasing degree were performed on a 100-subject database of three dimensional  $\delta B_0$  maps in the brain. The database was built from fieldmaps acquired on a MAGNETOM Prisma 3T imager (Siemens Healthcare GmbH, Erlangen, Germany) with 1.7 mm isotropic resolution, as already reported in [13]. Assuming no shimming of the brain would affect the quality of some  $\delta B_0$  maps with regards to distortion and signal loss, the fieldmaps were acquired subsequent to 2nd-order shimming by the Prisma scanner. This shim was based on the adjustment of a tilted bounding box adjacent to the brain from the initial 3-axis localizer images. In fact, the fieldmaps were obtained at the end of a 1-hour exam, provided there was some time left and the volunteer approved this last-minute acquisition.

To gain in  $\delta B_0$  precision, rather than using a double-echo gradient echo sequence, we opted for a triple-echo fieldmap acquisition scheme. In each brain voxel, potential temporal phase unwrapping between the second and third echoes was guided by the phase evolution between the first and second echoes, provided these were close enough such that no phase excursion could occur in-between beyond  $\pm\pi$ . This explains why fieldmap acquisitions were performed with two similar 3D gradient-echo sequences, one with 2 distant echoes  $TE_1 = 1.88$  ms and  $TE_3 = 4.9$  ms, and one with a single echo at  $TE_2 = TE_1 + 0.7$  ms. The 0.7 ms interval was picked by assuming  $\delta B_0$  does not exceed  $\pm 714$  Hz in the brain at 3 T. The sequences were played one after another and accelerated to last less than 45 s each, so that the risk of motion in-between was minimized. Then the slope of the phase evolution between  $TE_1$  and  $TE_2$  was extended for

phase unwrapping of the last echo, and a triple-point linear fit of the phase evolution was performed for  $\delta B_0$  estimation.

The resulting  $\delta B_0$  maps were cleaned with an outlier filter to avoid singularities, especially at the edge of the brain. The filter marked a brain voxel as outlier by comparing its excursion from the median to the variance, both statistics estimated from its neighbors; such outlier values were then replaced with their neighboring median. A mask of the brain was extracted from the magnitude image using FSL’s Brain Extraction Tool [34] to restrict our analysis solely to the human brain. The quality of the brain masks and fieldmaps was checked visually in at least the three orthogonal central slices for each subject.

$\delta B_0$  maps shimmed to 2<sup>nd</sup> degree presumably reflect magnetic susceptibility disparities in the head; they could be converted into ppm for the sake of generality. However since the UHF community is the main target of this study, we opted to report our simulation results at 7 T. So the  $\delta B_0$  maps, provided in Hz, were all scaled up by 7/3 for investigation at 7 T. Three typical B0 maps extracted from our 100-brain database are shown in Fig. 3 for information. They were picked to show B0 offsets in excess of 1000 Hz (at 7T), all located above the nasal sinus. Such values as well as the baseline average 65.7 Hz inhomogeneity may appear large compared to other values reported in the literature; this is partly due to the relatively high 1.7-mm image resolution which captures more finely the high susceptibility gradients at the brain interface.

### 3.3 Ultra-High-Degree Simulation of RSH Shimming

For the shimming simulations, given a target magnetic field  $\mathbf{b} \in \mathbb{R}^K$  across  $K$  voxels, the vector  $\mathbf{a} \in \mathbb{R}^{N^2+2N+1}$  of regular solid harmonic coefficients  $A_n^m$  for each degree  $n = 1, \dots, N$ , with  $N$  the RSH degree employed in the simulation,

is computed such that

$$\mathbf{a} = \underset{\mathbf{a} \in \mathbb{R}^{N^2+2N+1}}{\operatorname{argmin}} \quad \|\mathbf{b} - \mathbf{R}\mathbf{a}\|_2^2, \quad (17)$$

with  $\mathbf{R} \in \mathbb{R}^{K, N^2+2N+1}$  of the form

$$\mathbf{R} = \begin{bmatrix} \mathcal{R}_0^0(\mathbf{x}_1) & \mathcal{R}_1^{-1}(\mathbf{x}_1) & \mathcal{R}_1^0(\mathbf{x}_1) & \dots & \mathcal{R}_n^m(\mathbf{x}_1) & \dots & \mathcal{R}_N^N(\mathbf{x}_1) \\ \mathcal{R}_0^0(\mathbf{x}_2) & \mathcal{R}_1^{-1}(\mathbf{x}_2) & \mathcal{R}_1^0(\mathbf{x}_2) & \dots & \mathcal{R}_n^m(\mathbf{x}_2) & \dots & \mathcal{R}_N^N(\mathbf{x}_2) \\ \vdots & \vdots & \vdots & \ddots & \vdots & \ddots & \vdots \\ \mathcal{R}_0^0(\mathbf{x}_K) & \mathcal{R}_1^{-1}(\mathbf{x}_K) & \mathcal{R}_1^0(\mathbf{x}_K) & \dots & \mathcal{R}_n^m(\mathbf{x}_K) & \dots & \mathcal{R}_N^N(\mathbf{x}_K) \end{bmatrix}. \quad (18)$$

The inverse problem is solved using MATLAB's (The Mathworks, Natick, MA, USA) *lsqminnorm*.

For each subject, RSH shimming was performed targeting different types of brain regions: global, slice-by-slice and slab-specific. Slice-by-slice implies dynamic shimming of 1.7 mm transverse slices covering the whole-brain.

Slab-specific shimming was performed considering three different slabs containing notoriously challenging regions to shim, namely the prefrontal cortex (PFC) - because of its proximity to nasal and frontal sinuses, and the temporal lobes (TLs) - proximity to the inner ears. The choice of using slabs rather than employing precise segmentation of the regions of interest was made to account for common research and clinical practices. The 3 selected regions of the brain correspond to slabs that may be of interest when running high-resolution fMRI: suppose a 0.5 mm resolution is targeted at UHF, then the whole brain cannot be acquired in less than 3 s even with multiband accelerated EPI. Only a third of the brain might be achievable, which corresponds roughly to the size of the selected slabs. Neuroscientists may be interested solely in the PFC (e.g. to track decision-making processes), the temporal + parietal lobes (e.g. to

track the sense of spatial orientation), or the left TL (e.g. for language). Thus TL shimming was subdivided into two slab types: bilateral (including parietal lobes) and unilateral. Slab masks were created manually for each subject with approximate thickness of 55 mm. Shimming is performed on the voxels in the intersection of the slab with the brain mask. The targeted slab characteristics are shown in Fig. 4.

### 3.4 Verification of the conditions for ultimate shimming

As they support the theoretical demonstration that spherical regions of the brain that contain no magnetic source can be "perfectly" shimmed assuming the brain is a homogeneous medium, hypothetical spherical ROIs were defined in a single, randomly selected subject from the database, for proof-of-principle. Thus a spherical region enclosing critical inhomogeneity zones located in the ventral area of the prefrontal cortex, but not enclosing any obvious magnetic field sources (air cavities) is first selected for validation of the condition for perfect shimming. RSH shimming of increasing degree is performed inside this ROI and it is compared to the achieved inhomogeneity for the same subject under global shimming. The spherical ROI is then shifted downward along the Head-Feet direction, and RSH shimming is applied on the voxels in the intersection of the brain mask with the ROI ( $\rightarrow$  truncated sphere). If the proposed condition for ultimate shimming is consistent, the sphere entirely located inside the brain should provide better homogeneity than the subsequent truncated spheres. The spherical ROI has 38 mm radius and is shown in Fig. 5.

### 3.5 Optimal cylindrical shim coil design

In order to explore practical aspects of coil design, and how realistic cylindrical systems could perform relatively to the best achievable inhomogeneity, the



Dipole Boundary Method (DBM) [13] is applied to compute subject-optimal stream-functions (SO-SFs) for each subject in the database under global and slab-specific shimming techniques.

SO-SFs are computed under different power dissipation targets to assess how performances relative to the best achievable homogeneity estimated from RSH shimming simulations are impacted by engineering limitations.

Based on our previous work and on a home-made 27-cm diameter parallel transmit head coil [13, 14], the SO-SFs are calculated over a cylindrical coil former of 140 mm radius, 300 mm length, with a 4 mm discretization step. Discretization into windings is performed with 2.4 mm minimum inter-wire spacing and copper wire of  $1.54 \text{ mm}^2$  circular section. Power dissipation for each coil is then calculated for the obtained winding pattern. Target power for the designs are 3 W, 7 W, 15 W, 25 W, 50 W, 75 W and 100 W. For information, examples of SO-SF coil patterns already reported in our previous work [13] are recalled in Fig. 6. Such patterns are used for simulations presented herein, whereby inhomogeneity levels resulting from subject optimal designs are assessed and compared to very high-degree RSH shimming limits.

## 4 Results and Discussion

### 4.1 Magnetic Field Perturbation Sources in the Human Head

The disposition of points  $\mathbf{x}$  satisfying  $\rho_m(\mathbf{x}) \neq 0$  is shown in Fig. 7. A build-up of susceptibility-induced field sources is observed on the interface between the head and the surrounding air. Closer to the brain are the susceptibility-induced sources caused by susceptibility gradients between air cavities in the head (sinus and ear canals) and biological tissues. It is also apparent that, under the displayed configuration, the condition for perfect shimming cannot

be fulfilled as the ball  $\mathcal{B}(\text{inf } \mathcal{X}, \mathcal{O})$  will not enclose the brain. Or, alternatively, it is impossible to obtain any brain-enclosing sphere that does not enclose perturbation sources.

The distribution of perturbation sources estimated from equation 2 is compatible with the strong inhomogeneous magnetic field commonly observed in the temporal lobes and frontal lobe. These inhomogeneity hotspots are discussed throughout a vast literature, from simulated [30, 35, 36] to measured data [37, 38]. Due to the proximity of the sources to the brain, intense magnetic field values appear in the brain cortex, reaching values as high as 800 Hz at 7 T, as gathered from the database.

## 4.2 Whole-brain B0 Homogeneity Limits

The results for human brain shimming with very high RSH degree are shown in Fig. 8. Baseline inhomogeneity across the database is 65.7 Hz (SD: 11.4 Hz). As RSH degree increases, a steep inhomogeneity drop is observed up to 20<sup>th</sup> degree, with the rate of improvement of 1.5 Hz per degree when around 10<sup>th</sup> degree and a contrasting slower improvement afterwards, with only 0.07 Hz per degree around 70<sup>th</sup> degree. Due to limited computational resources and time, the maximum RSH degree was increased up to 90, presenting inhomogeneity of 15.9 Hz (SD: 3.4 Hz) in the brain, or an improvement of 75.8 % relative to baseline.

Consistent with theoretical developments, an asymptotic behavior, tending to non-zero inhomogeneity, can be inferred from the inhomogeneity evolution. The minimum inhomogeneity achievable in the database could be extrapolated using MATLAB’s *Curve Fitting Tool*, providing an average 12.3 Hz (95 % Confidence Bounds: 10.9 Hz–13.7 Hz) for the database. This value represents an 81.3 % improvement in homogeneity in the human brain. In theory, this

result indicates that inhomogeneity at UHF of 7 T and 11.7 T could be reduced to the equivalent of 1.4 T and 2.4 T MRI systems, respectively, although the practical implementation of such a system is very unlikely.

From Fig. 8a, it can also be noticed that a 2nd-order simulated re-shim improved the experimental baseline shim by roughly 10%. Two factors may explain this difference: first the brain is not masked by the scanner software, so voxels in the bounding box outside the brain may contribute to suboptimal brain shimming. Second, potential patient motion between the shimming procedure and the B0 map acquisition (1-hour delay) may modify the B0 map and deteriorate the shim. Thus our reference fieldmaps were not fully corrected for 2nd-order SH, which explains why a post-exam theoretical 2nd-order re-shim results in a better B0 homogeneity.

Since our reference database is not flawless with respect to the 2<sup>nd</sup>-degree baseline shim, the relative SH inhomogeneity improvements provided here should be considered with caution. Nevertheless, our absolute inhomogeneity results remain valid as they could be corroborated by experimental works (e.g. [14, 15]); in particular, the  $\sim 12$  Hz homogeneity limit should presumably be invariant to the baseline. QSM and other methods have shown that gray/white matter differences can easily account for 5 Hz of inhomogeneity, which would account for  $\sim 17\%$  of the stated limit (assuming quadratic contributions). Presumably, the remaining  $\sim 11$  Hz contribution could then be explained by the air-induced non-recoverable residuals.

Regarding the voxels presenting absolute field excursion superior to 100 Hz, which would account for stronger  $B_0$  related artifacts, it follows a similar trend to that of the inhomogeneity, reaching a virtually artifact-free configuration, as an average of less than 0.5% of voxels over 100 Hz is achieved. This reduction is dramatic relatively to the initial proportion of 7.8%, which may cause

information in a non-negligible portion of the brain to be lost in an EPI scan, for instance.

A more detailed visualization of how increasing RSH degrees act to reduce global inhomogeneity is provided in Fig. 9, where the evolution of the maximum  $|\delta B_0|$  for the 80, 90, 95 and 98 % voxels with lowest absolute excursion is shown. At relatively lower degrees, RSH functions act over all frequency ranges. As the correction degree increases, RSH action seems to be localized, as significant changes are mostly observed in the 95 and 98 % ranges, thus on a smaller amount of voxels.

Fig. 10 shows that strong inhomogeneity regions still remain even after global shimming at very high degree. And although inhomogeneity values at very high degree present a significant drop from baseline inhomogeneity, most shim systems presented in the literature have shown performances at most equivalent to 6<sup>th</sup> degree RSH despite optimization of MCA loops placement and geometry in some studies [11, 29, 39].

In slice-by-slice shimming (cf Fig. 8b), inhomogeneity reduction as RSH degree increases is much greater. Inhomogeneity at 17<sup>th</sup> degree is 12.6 Hz (SD: 3.4 Hz), and already inferior to the inhomogeneity at 90<sup>th</sup> degree in global shimming. Voxels over 100 Hz are reduced to 0.2 % (SD: 0.1 %). The greater effectiveness of dynamic slice-by-slice shimming in mitigating  $B_0$  inhomogeneity when compared to global shimming is known [8, 40], and it is what makes it appealing for 2D acquisition schemes. From the results, we see that such a feature is linked to the lower RSH degree required, which indicates that less rapid spatial field variation is needed. From a shim system design perspective, given some surface upon which wire patterns will be placed, being able to generate rapidly spatially varying fields means putting as many loops as possible covering the whole surface. These RSH simulations indicate that the

same spatial distribution of coils in a Multi-Coil Array will be able to perform better in slice-by-slice shimming compared to global shimming due to the need of lower degree RSH. While an efficient technique for reducing inhomogeneity, if isotropic submillimeter resolution is desired, 2D acquisition of very thin slices might not provide sufficient SNR. Three-dimensional acquisitions become necessary, and global shimming could be required.

### 4.3 Slab Shimming Limits

While slice-by-slice shimming might be unsuited for submillimeter resolution, slab-specific acquisition can be a viable alternative if only a specific region of the brain is of interest. Figs. 11 and 12 show that this shimming modality could also improve homogeneity given a fixed degree of RSH components when compared to what would be achieved in the same ROI under global shimming. Fig. 12 shows that at 3<sup>rd</sup> degree (which is available to limited order in some UHF scanners), localized shimming in specific slabs could provide significant inhomogeneity reduction, with average drops of 7.7 Hz, 9.0 Hz and 8.0 Hz in the PFC and TLs (bilateral and unilateral), respectively. Moreover, considering the TL bilateral slab, when applying global shimming, a 6<sup>th</sup> degree RSH shim system would be required to provide the same homogeneity as a 3<sup>rd</sup> degree system if localized shimming was employed. From a hardware perspective, going from 3<sup>rd</sup> to 6<sup>th</sup> degree implies adding 33 coils. Therefore, great economy of resources is possible by changing the shimming strategy, provided whole-brain shimming is not an issue. It can also be noticed from the localized shimming simulations that global shimming seems to naturally concentrate efforts in mitigating inhomogeneity in the PFC, as there is a smaller gap in performance and coil number when switching from global to localized shimming. Such smaller relative improvements in the temporal lobes homogeneity

has been noticed in several works [11, 26, 41], but as can be seen, could be overcome if localized shimming was employed.

None of the shimming schemes presented so far satisfies the condition for ultimate shimming. In average, the residual inhomogeneity observed in the shimmed ROIs is still superior to 10 Hz.

One limitation of slab shimming (and, to a lesser extent, of slice-by-slice shimming) is the unwanted selection of out-of-slab voxels, upon which no control of the B0 field has been imposed. These may indeed fold back into the FOV if slab selection is not properly handled. Here we implicitly assume slab selection is carefully handled by multidimensional tailored RF pulse/gradient design which would take such tricky voxels into account. Alternatively, in the framework of a conventional slab selection, the shimming problem may embed a constraint on out-of-slab voxels to ensure that the given slab selection gradient would exclude them from the RF pulse bandwidth.

#### 4.4 Towards Perfect Shimming in Spherical ROIs

To further study the validity and consequences of the perfect shimming condition, RSH shimming simulations were performed in the four distinct ROIs shown in Fig. 5. We notice how RSH shimming in ROIs 3 and 4, which presumably satisfy the perfect shimming condition, converge faster to lower inhomogeneity values (8.0 Hz and 4.5 Hz, respectively) as RSH degree is increased, and present a more localized residual inhomogeneity compared to ROIs 1 and 2 (with final inhomogeneity of 32.7 Hz and 23.0 Hz, respectively). Nevertheless, residual inhomogeneity in ROIs 3 and 4 still remains. With more harmonic terms and enough numerical precision to compute them, the residual “stains” close to the nasal sinus air cavity are expected to vanish in those

ROIs. Nevertheless, in that case, smaller residuals reflecting internal brain susceptibility disparities would still remain, since these cannot be compensated for by shimming.

Moreover, contrarily to intuition, these results also show that fitting the same number of degrees of freedom to a smaller volume does not necessarily mean improved shimming, since despite being the smallest volume, ROI 1 is also the one presenting the largest field excursion in the depicted sagittal slices. Fig. 5c compares the inhomogeneity inside ROI 4 when applying global vs focused shimming: convergence to very low inhomogeneity is seen at 10<sup>th</sup> degree with localized shimming, versus 50<sup>th</sup> degree with global shimming.

In terms of the required RSH degree for optimally shimming some region, presented results point to the need of fewer degrees of freedom when employing localized shimming, and these can be further reduced when the shimmed ROI can be positioned inside a sphere non enclosing sources of magnetic field.

## 4.5 Optimal Global and Localized Shimming with Power Constraints

The reduced number of degrees of freedom is a first practical aspect pointing to the advantage of localized shimming. Moreover, by analyzing the inhomogeneity reduction brought by optimal, power-constrained coil designs, the reduced need for RSH degrees in localized shimming translates into improved homogeneity in the target under fixed power dissipation, as observed in Fig. 13.

Inhomogeneity after global shimming with subject-optimal coils at the initial power constraint of 3W is equivalent to 6<sup>th</sup> degree RSH shimming. Improvement as power consumption is allowed to increase, however, is mild,

reaching an equivalent of a 9<sup>th</sup> degree RSH shim system at 100 W. As inhomogeneous field distribution becomes more and more localized after mitigation of slower spatially varying patterns, further improvement becomes harder. To address such localized patterns when performing global shimming, small loops with high electric current are needed, thus electric power drastically increases. Such behavior is in accordance with [21], who demonstrates that pure higher degree spherical harmonic patterns are generated by faster spatially varying, thus shorter, winding patterns, at the cost of requiring higher currents.

Subject-optimal coil design for localized shimming, however, shows that a significant 17% drop in inhomogeneity can be achieved for the temporal lobes under the same power dissipation constraints with a dedicated system. From the results discussed so far, this is not surprising; for a fixed RSH degree, localized shimming improves the homogeneity in the target compared to global shimming; and since power dissipation is linked to RSH content, employing the same power dissipation in a localized target rather than in global shimming is the equivalent of employing the same amount of RSH degrees in localized versus global shimming. From these results, one could also expect high performance shimming in spherical ROIs satisfying the perfect shimming conditions to be achievable with low power consumption, as the RSH content required to achieve the lowest inhomogeneity in ROI 4, for instance, is of 10<sup>th</sup> degree, with still very low inhomogeneity at the 6<sup>th</sup> degree.

We emphasize that the coil design simulation and evaluation had the goal of illustrating how RSH degree content relates to power dissipation. The designed systems are not practical as they imply an optimal coil for each subject. When designing a shim system capable of addressing inter-subject variability, for a fixed power dissipation, performances tend to drop [13]. Nevertheless,



these simulations provided evaluation of how power capabilities can be better redirected to improve homogeneity of specific regions of interest.

We also note that, despite the low inhomogeneity theoretically achievable in global shimming, in practice such levels of inhomogeneity are probably not achievable since dedicated hardware might not be able to support current and power levels required to generate the correcting magnetic fields. At 100 W, average inhomogeneity of 39.3 Hz obtained under global shimming is only equivalent to what would be obtained with 9<sup>th</sup> degree RSH shimming, thus still very far from the estimated lower bound of 12.3 Hz.

Finally, the shimming needs will mainly depend on the robustness of the acquisition sequence to  $B_0$  inhomogeneity. Acquisition schemes such as GRE, MP-RAGE, FSE provide high quality results at 7 T despite conditions that would be harsh for EPI; therefore for those sequences one would not need the best achievable inhomogeneity. For EPI, however, even at 90<sup>th</sup> degree RSH shimming, leftover inhomogeneity hotspots would still translate into artifacts if no acceleration was used. Again for high-resolution and reduced FOV, localized shimming will facilitate greater shimming performance.

## 5 Conclusion

### 5.1 Ultimate whole-brain shim limits

The mathematical fundamentals pointing to the impossibility of perfect shimming of the human brain were shown, and unconstrained RSH shimming simulations of very high degree were performed, showing reminiscent regions of high magnetic field excursion at 7 T even at the highest degree simulated, demonstrating the impossibility of perfect shimming of the human brain (12.3 Hz remaining inhomogeneity in average across a 100-subject database). Could the brain be approximated as a magnetic homogeneous medium, it

would be possible to perfectly shim spherical regions inside it. On the other hand, we demonstrate that air cavities within concave regions of the brain make perfect shimming impossible when the spherical ROI encapsulates such cavities.

## 5.2 Towards practical optimal brain shimming

Conventional generic shim systems correcting for SH variations up to  $n^{\text{th}}$ -order need  $(n + 1)^2 - 1$  coils on top of one-another. Beyond  $n = 4$ , they would require a far too extreme number of coils and are therefore excluded to tackle very high-degree shimming. Yet in parallel with other teams [12, 42], we recently showed that by specifically targeting the human brain, it is possible to achieve the performance of high-order SH systems with much fewer coils than generic SH-correcting coils [13]. For instance, in Fig. 8 of the latter reference, a 5-coil system with limited power ( $< 60$  W) is demonstrated to reach the same performance as 27 SH coils with unlimited power.

Nevertheless, an optimized close-to-ideal cylindrical shim coil here showed inhomogeneity only comparable to a  $9^{\text{th}}$  degree RSH shim system, despite rather high power dissipation of 100 W. This result helps highlight the difficulty of obtaining high performance shim systems with low power consumption, and sheds light on why, despite efforts developed by many research teams, no system performing better than  $6^{\text{th}}$  degree has been prototyped so far. Indeed up-to  $6^{\text{th}}$  degree performance can be reached by compact state-of-the-art MCAs [11, 14, 41, 43], yielding a 35% inhomogeneity reduction. MCAs come with their share of challenges such as coil-to-coil interactions, gradient-induced eddy currents and shim preemphasis compensation, which can be tackled by appropriate feedback electronics (e.g. [44]). Then high-power high-cost systems such as those presented in [13] may be built to reach 10th-order SH shimming,

with a 10 % extra gain in inhomogeneity reduction, but beyond 10th-order, the gain is probably not worth the effort, considering the amount of coils, maximum intensity and power that will be needed to operate the system. However, this statement holds for the whole brain. As explained hereby, if only part of the brain is of interest, more gain is to be achieved by considering shim coils dedicated to specific cerebral regions.

### **5.3 Shim systems dedicated to localized shimming improve performance**

Localized shimming was shown to provide better homogeneity in a target region than global shimming for a fixed RSH degree. This property was reflected in greater performance of localized shimming under a fixed power dissipation condition.

By judiciously selecting a region to shim such that it satisfies the condition of being enclosed by a sphere not containing sources of magnetic field, very low inhomogeneity can be achieved within relatively low RSH degree, as we observed a faster convergence to the lowest achievable inhomogeneity; in this particular case, the latter is left with lower field excursion caused by less intense susceptibility gradients between tissues composing the brain. We would therefore expect rather low power requirements for shimming systems to achieve almost optimal inhomogeneity in such targets.

## **Acknowledgements**

We would like to thank Nicolas Boulant and Guy Aubert for helpful discussions on this subject.

Funding: This work was supported by the Commissariat à l’Energie Atomique et aux Energies Alternatives (CEA) through a PhD scholarship.

## References

- [1] Salomir, R., de Senneville, B.D., Moonen, C.T.: A fast calculation method for magnetic field inhomogeneity due to an arbitrary distribution of bulk susceptibility. *Concepts in Magnetic Resonance Part B: Magnetic Resonance Engineering* **19B**(1), 26–34 (2003)
- [2] Lüdeke, K.M., Röschmann, P., Tischler, R.: Susceptibility artefacts in NMR imaging. *Magnetic Resonance Imaging* **3**(4), 329–343 (1985). [https://doi.org/10.1016/0730-725X\(85\)90397-2](https://doi.org/10.1016/0730-725X(85)90397-2)
- [3] Jezzard, P., Balaban, R.S.: Correction for geometric distortion in echo planar images from B<sub>0</sub> field variations. *Magnetic Resonance in Medicine* **34**(1), 65–73 (1995). <https://doi.org/10.1002/mrm.1910340111>
- [4] Zhao, Y., Anderson, A.W., Gore, J.C.: Computer simulation studies of the effects of dynamic shimming on susceptibility artifacts in EPI at high field. *Journal of Magnetic Resonance* **173**(1), 10–22 (2005). <https://doi.org/10.1016/j.jmr.2004.11.009>
- [5] Koch, K.M., Rothman, D.L., de Graaf, R.A.: Optimization of static magnetic field homogeneity in the human and animal brain in vivo. *Progress in Nuclear Magnetic Resonance Spectroscopy* **54**(2), 69–96 (2009). <https://doi.org/10.1016/j.pnmrs.2008.04.001>
- [6] Smith, T.B., Nayak, K.S.: MRI artifacts and correction strategies. *Imaging in Medicine* **2**(4), 445–457 (2010). <https://doi.org/10.2217/iim.10.33>
- [7] Mullen, M., Garwood, M.: Contemporary approaches to high-field magnetic resonance imaging with large field inhomogeneity. *Progress in*

- Nuclear Magnetic Resonance Spectroscopy **120-121**, 95–108 (2020).  
<https://doi.org/10.1016/j.pnmrs.2020.07.003>. Accessed 2021-01-07
- [8] Juchem, C., Nixon, T.W., McIntyre, S., Boer, V.O., Rothman, D.L., Graaf, R.A.d.: Dynamic multi-coil shimming of the human brain at 7T. *Journal of Magnetic Resonance* **212**(2), 280–288 (2011). <https://doi.org/10.1016/j.jmr.2011.07.005>
- [9] Stockmann, J., Witzel, T., Blau, J., Polimeni, J., Wei, Z., Keil, B., Wald, L.: Combined shim-rf array for highly efficient shimming of the brain at 7 tesla. *Proc. Int. Soc. Magn. Reson. Med* **21** (2013)
- [10] Juchem, C., Umesh Rudrapatna, S., Nixon, T.W., de Graaf, R.A.: Dynamic multi-coil technique (DYNAMITE) shimming for echo-planar imaging of the human brain at 7 Tesla. *NeuroImage* **105**, 462–472 (2015). <https://doi.org/10.1016/j.neuroimage.2014.11.011>. Accessed 2019-10-27
- [11] Aghaeifar, A., Zhou, J., Heule, R., Tabibian, B., Schölkopf, B., Jia, F., Zaitsev, M., Scheffler, K.: A 32-channel multi-coil setup optimized for human brain shimming at 9.4T. *Magnetic Resonance in Medicine* **83**(2), 749–764 (2020). <https://doi.org/10.1002/mrm.27929>. Accessed 2020-08-11
- [12] Jia, F., Elshatlawy, H., Aghaeifar, A., Chu, Y., Hsu, Y., Littin, S., Kroboth, S., Yu, H., Amrein, P., Gao, X., Yang, W., LeVan, P., Scheffler, K., Zaitsev, M.: Design of a shim coil array matched to the human brain anatomy. *Magnetic Resonance in Medicine* **83**(4), 1442–1457 (2020). <https://doi.org/10.1002/mrm.28016>. Accessed 2020-08-11
- [13] Pinho Meneses, B., Amadon, A.: A fieldmap-driven few-channel shim coil

- design for MRI of the human brain. *Physics in Medicine & Biology* **66**(1) (2020)
- [14] Pinho Meneses, B., Stockmann, J., Chazel, E., Giacomini, E., Gapais, P.-F., Mauconduit, F., Luong, M., Vignaud, A., Amadon, A.: Shim Coils Tailored for Correction of B0 Inhomogeneity in the Human Brain (SCOTCH) at Ultra High Field. In: *Proc. Int. Soc. Magn. Reson. Med.*, vol. 29. Virtual Conference, p. 3107 (2021). <https://index.miramart.com/ISMRM2021/PDFfiles/3107.html>
- [15] Pinho Meneses, B.: Static field shimming in the human brain for ultra-high field MRI : conceptual limits and development of a novel hardware prototype. PhD thesis, Université Paris-Saclay (2021)
- [16] Damme, L.V., Mauconduit, F., Chambrion, T., Boulant, N., Gras, V.: Universal nonselective excitation and refocusing pulses with improved robustness to off-resonance for Magnetic Resonance Imaging at 7 Tesla with parallel transmission. *Magnetic Resonance in Medicine* **85**(2), 678–693 (2021). <https://doi.org/10.1002/mrm.28441>. Accessed 2021-03-03
- [17] Juchem, C., Cudalbu, C., Graaf, R.A.d., Gruetter, R., Henning, A., Hetherington, H.P., Boer, V.O.: B0 shimming for in vivo magnetic resonance spectroscopy: Experts’ consensus recommendations. *NMR Biomed* **34**(5), 4350 (2020). <https://doi.org/10.1002/nbm.4350>. Accessed 2021-02-02
- [18] Sadeghi-Tarakameh, A., DelaBarre, L., Lagore, R.L., Torrado-Carvajal, A., Wu, X., Grant, A., Adriany, G., Metzger, G.J., Moortele, P.-F.V.d., Ugurbil, K., Atalar, E., Eryaman, Y.: In vivo human head MRI at 10.5T: A radiofrequency safety study and preliminary imaging results. *Magnetic Resonance in Medicine* **84**(1), 484–496 (2020). <https://doi.org/10.1002/>

[mrm.28093](#). Accessed 2021-01-23

- [19] Quettier, L., Aubert, G., Belorgey, J., Berriaud, C., Bredy, P., Dilasser, G., Dubois, O., Gilgrass, G., Guihard, Q., Jannot, V., Juster, F.-P., Lannou, H., Molinie, F., Nunio, F., Roger, A., Schild, T., Scola, L., Sinanna, A., Stepanov, V., Vedrine, P.: Commissioning Completion of the Iseult Whole Body 11.7 T MRI System. *IEEE Transactions on Applied Superconductivity* **30**(4), 1–5 (2020). <https://doi.org/10.1109/TASC.2020.2983702>. Accessed 2020-11-30
- [20] Bandettini, P.A.: Twenty years of functional MRI: The science and the stories. *NeuroImage* **62**(2), 575–588 (2012). <https://doi.org/10.1016/j.neuroimage.2012.04.026>. Accessed 2021-01-23
- [21] Roméo, F., Hoult, D.I.: Magnet field profiling: Analysis and correcting coil design. *Magnetic Resonance in Medicine* **1**(1), 44–65 (1984). <https://doi.org/10.1002/mrm.1910010107>
- [22] De Graaf, R.A.: *In Vivo NMR Spectroscopy: Principles and Techniques*, 2nd ed edn. John Wiley & Sons, Chichester, West Sussex, England ; Hoboken, NJ (2007)
- [23] Webb, A. (ed.): *Magnetic Resonance Technology: Hardware and System Component Design*. New developments in NMR, vol. 7. Royal Society of Chemistry, Cambridge, UK (2016)
- [24] Pan, J.W., Lo, K.-M., Hetherington, H.P.: Role of very high order and degree B<sub>0</sub> shimming for spectroscopic imaging of the human brain at 7 tesla. *Magnetic resonance in medicine* **68**(4), 1007–1017 (2012). <https://doi.org/10.1002/mrm.24122>

- [25] Han, H., Song, A.W., Truong, T.-K.: Integrated parallel reception, excitation, and shimming (iPRES): Integrated Parallel Reception, Excitation, and Shimming. *Magnetic Resonance in Medicine* **70**(1), 241–247 (2013). <https://doi.org/10.1002/mrm.24766>. Accessed 2020-08-11
- [26] Aghaeifar, A., Mirkes, C., Bause, J., Steffen, T., Avdievitch, N., Henning, A., Scheffler, K.: Dynamic B0 shimming of the human brain at 9.4 T with a 16-channel multi-coil shim setup. *Magnetic Resonance in Medicine* **80**(4), 1714–1725 (2018). <https://doi.org/10.1002/mrm.27110>. Accessed 2019-09-03
- [27] Meneses, B.P., Luong, M., Amadon, A.: Optimized multi-coil array design for human brain shimming at Ultra-High Field. In: *Proc. Intl. Soc. Mag. Reson. Med*, vol. 27. Montreal, Canada, p. 1477 (2019). <https://index.mirasmart.com/ISMRM2019/PDFfiles/1477.html>
- [28] Pinho Meneses, B., Amadon, A.: Static-magnetic-field Shimming Coil System for Magnetic Resonance Imaging, Patent Pending in Europe and The USA. EP-3726238-A1, October 2020. <https://app.dimensions.ai/downloads/patents?ucid=EP-3726238-A1>
- [29] Pinho Meneses, B., Stockmann, J., Amadon, A.: First prototype of a Stream-Function-based Multi-Coil Array dedicated to human brain shimming at Ultra-High-Field. In: *Proc.Intl.Soc.Mag.Reson.Med*, vol. 28. Virtual, p. 0766 (2020). <https://index.mirasmart.com/ISMRM2020/PDFfiles/0766.html>
- [30] Hillenbrand, D.F., Lo, K.M., PUNCHARD, W.F.B., Reese, T.G., Starewicz, P.M.: High-order MR shimming: a simulation study of the effectiveness of competing methods, using an established susceptibility model of the



- human head. *Applied Magnetic Resonance* **29**(1), 39–64 (2005). <https://doi.org/10.1007/BF03166955>. Accessed 2021-01-10
- [31] Duyn, J.H., Schenck, J.: Contributions to magnetic susceptibility of brain tissue. *NMR Biomed* **30**(4), 3546 (2017)
- [32] Jackson, J.D.: *Classical Electrodynamics*, 3rd edn. John Wiley & Sons, Inc, Hoboken, NJ (1999)
- [33] Makris, N., Angelone, L., Tulloch, S., Sorg, S., Kaiser, J., Kennedy, D., Bonmassar, G.: MRI-based anatomical model of the human head for specific absorption rate mapping. *Medical & Biological Engineering & Computing* **46**(12), 1239–1251 (2008). <https://doi.org/10.1007/s11517-008-0414-z>. Accessed 2020-11-30
- [34] Smith, S.M.: Fast robust automated brain extraction. *Human Brain Mapping* **17**(3), 143–155 (2002). <https://doi.org/10.1002/hbm.10062>
- [35] Li, S., Williams, G.D., Frisk, T.A., Arnold, B.W., Smith, M.B.: A computer simulation of the static magnetic field distribution in the human head. *Magnetic Resonance in Medicine* **34**(2), 268–275 (1995). <https://doi.org/10.1002/mrm.1910340219>. Accessed 2021-01-24
- [36] Kochan, M., Daga, P., Burgos, N., White, M., Cardoso, M.J., Mancini, L., Winston, G.P., McEvoy, A.W., Thornton, J., Yousry, T., Duncan, J.S., Stoyanov, D., Ourselin, S.: Simulated field maps for susceptibility artefact correction in interventional MRI. *International Journal of Computer Assisted Radiology and Surgery* **10**(9), 1405–1416 (2015). <https://doi.org/10.1007/s11548-015-1253-7>. Accessed 2021-01-24

- [37] Li, S., Dardzinski, B.J., Collins, C.M., Yang, Q.X., Smith, M.B.: Three-dimensional mapping of the static magnetic field inside the human head. *Magnetic Resonance in Medicine* **36**(5), 705–714 (1996). <https://doi.org/10.1002/mrm.1910360509>. Accessed 2021-01-24
- [38] Collins, C.M., Yang, B., Yang, Q.X., Smith, M.B.: Numerical calculations of the static magnetic field in three-dimensional multi-tissue models of the human head. *Magnetic Resonance Imaging* **20**(5), 413–424 (2002). [https://doi.org/10.1016/S0730-725X\(02\)00507-6](https://doi.org/10.1016/S0730-725X(02)00507-6). Accessed 2021-01-24
- [39] Zhou, J., Stockmann, J.P., Arango, N., Witzel, T., Scheffler, K., Wald, L.L., Lin, F.: An orthogonal shim coil for 3T brain imaging. *Magnetic Resonance in Medicine* **83**(4), 1499–1511 (2020). <https://doi.org/10.1002/mrm.28010>. Accessed 2021-01-08
- [40] Koch, K.M., McIntyre, S., Nixon, T.W., Rothman, D.L., de Graaf, R.A.: Dynamic shim updating on the human brain. *Journal of Magnetic Resonance* **180**(2), 286–296 (2006). <https://doi.org/10.1016/j.jmr.2006.03.007>. Accessed 2021-02-13
- [41] Stockmann, J.P., Wald, L.L.: In vivo B<sub>0</sub> field shimming methods for MRI at 7 T. *NeuroImage* **168**, 71–87 (2018). <https://doi.org/10.1016/j.neuroimage.2017.06.013>. Accessed 2019-10-08
- [42] Arango, N., Stockmann, J.P., Adalsteinsson, E., White, J.: Ultimate B<sub>0</sub> Shim and the Design of Optimal Shim Bases. In: *Proc. Int. Soc. Magn. Reson. Med*, vol. 27, p. 1462 (2019). <https://index.mirasmart.com/ISMRM2019/PDFfiles/1462.html>
- [43] Juchem, C., Green, D., de Graaf, R.A.: Multi-coil magnetic field modeling.

Journal of Magnetic Resonance **236**, 95–104 (2013). <https://doi.org/10.1016/j.jmr.2013.08.015>. Accessed 2021-01-07

- [44] Arango, N., Stockmann, J.P., Witzel, T., Wald, L.L., White, J.: Open-source, low-cost, flexible, current feedback-controlled driver circuit for local B<sub>0</sub> shim coils and other applications. In: Proc. Int. Soc. Magn. Reson. Med, vol. 24, p. 1157 (2016). <https://cds.ismrm.org/protected/16MProceedings/PDFfiles/1157.html>

# List of Figures

1	(a) Disposition of fundamental building blocks for sample-induced magnetic field perturbation ( $\mathbf{m}_p$ ) and field correction ( $I_c d\mathbf{l}$ ) around the brain. The MR magnet isocenter at $\mathcal{O}$ corresponds to the origin of the $B_0$ SH-decomposition. Vector $\mathbf{x} \in \mathbb{R}^3$ points to an arbitrary brain voxel to be shimmed. (b) A representation of the regions where the magnetic field generated by a punctual sample-induced perturbation is described by RSH ( $\mathcal{V}_<^p$ ) and ISH ( $\mathcal{V}_>^p$ ). (c) The region $\mathcal{V}_<^c$ where the correction magnetic field is decomposed into RSH. . . . .	6
2	Examples of Spherical Harmonic functions of various degrees and orders (cf. equation 7). . . . .	8
3	Examples of brain $B_0$ maps from our 100-subject database (in Hz, rescaled at 7T, with 1.7-mm isotropic resolution) showing excursions above 1000 Hz, always in the olfactory lobe. The displayed gray scales extend from the minimum to the maximum $B_0$ -offset in each whole brain. The three depicted orthogonal slices (respectively sagittal, axial, coronal) are those going through the maximum-value voxel in each case. . . . .	38
4	Slab positioning for localized shimming . . . . .	39
5	Inhomogeneity assessment after shimming in four spherical ROIs, with ROIs 3 and 4 non-enclosing magnetic field sources, and ROIs 1 and 2 virtually enclosing such sources. Inhomogeneity as RSH degree increases (a) and fieldmap in a sagittal slice after 50 <sup>th</sup> degree shimming (b) are shown. Inhomogeneity evolution inside ROI 4 is also compared under localized and global shimming (c). . . . .	40

6	Wire geometric centers of subject-optimal coils for 3 subjects at two different performances and power dissipation for each subject. The colormap represent the Stream Function intensity around the cylindrical surface (red is positive, blue is negative, which gives the sign of the current flow in the depicted windings)[13]. . . . .	41
7	Magnetic field source disposition around the human brain as computed from equation 2. The deep red color is representative of a large susceptibility laplacian coming from the difference between air and tissue susceptibilities, typically an order-of-magnitude above the inner tissue disparities. The associated voxels are those in contact with air in head cavities (inner ear canals, sinus...). Amongst them, those close to or in contact with the brain contribute to the main B0-field inhomogeneities therein. . . . .	41
8	Final inhomogeneity and percentage of voxels of 100 Hz after global and slice by slice RSH shimming . . . . .	42
9	Average frequency span after RSH shimming of increasing degree	43
10	Selected axial slices of brain fieldmap after RSH global shimming of different degrees. The slices show zones of high inhomogeneity. 4 <sup>th</sup> and 6 <sup>th</sup> degree fieldmaps are shown as examples of the maximum mitigation levels achieved by shimming systems so far as reported in the literature when performing global shimming. The best inhomogeneity obtained (90 <sup>th</sup> degree shimming) in our unconstrained simulations is also shown. . . . .	44
11	Final inhomogeneity and percentage of voxels of 100 Hz within target slabs after localized and global RSH shimming . . . . .	45

12	Detailed performance comparison between global and localized shimming techniques . . . . .	46
13	Average inhomogeneity across fieldmaps for subject-optimal coil shimming designed for global and localized shimming as a function of power dissipation . . . . .	47

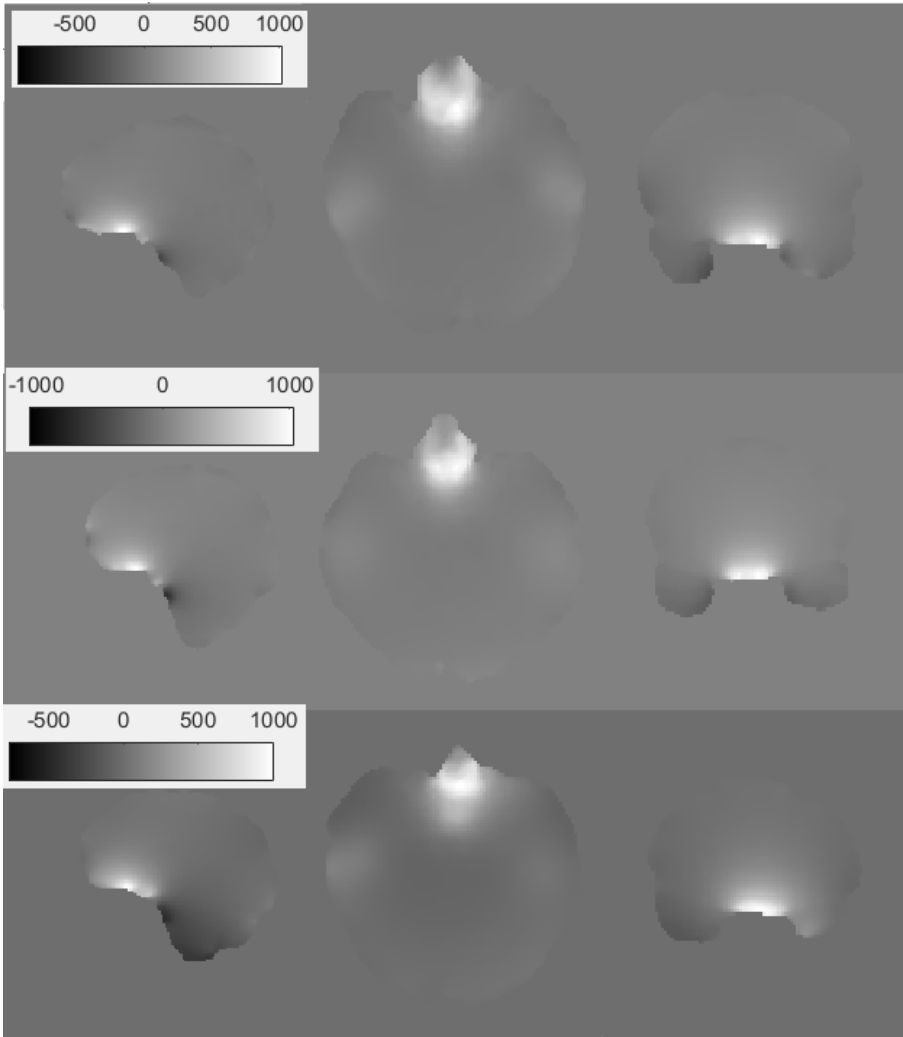


**Fig. 3:** Examples of brain B0 maps from our 100-subject database (in Hz, rescaled at 7T, with 1.7-mm isotropic resolution) showing excursions above 1000 Hz, always in the olfactory lobe. The displayed gray scales extend from the minimum to the maximum B0-offset in each whole brain. The three depicted orthogonal slices (respectively sagittal, axial, coronal) are those going through the maximum-value voxel in each case.

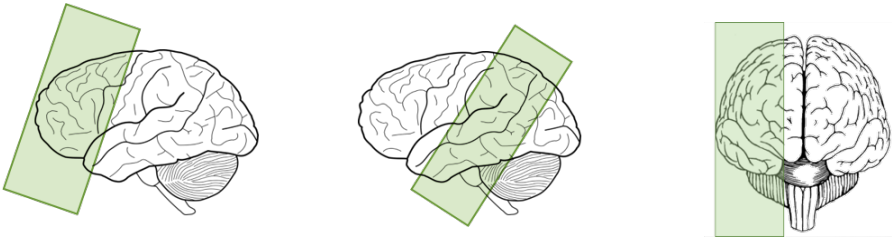
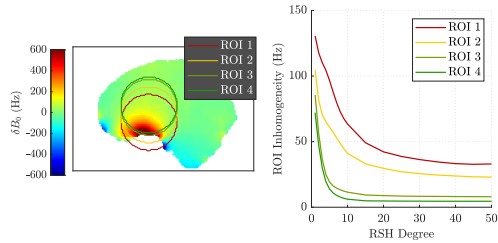
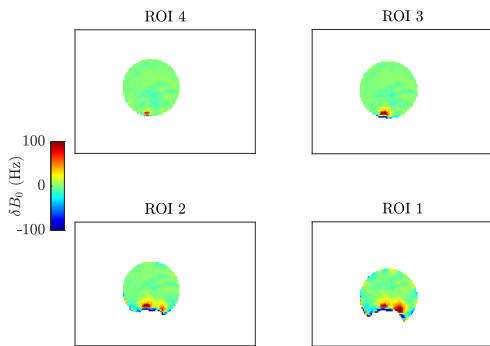


**Fig. 4:** Slab positioning for localized shimming simulations with RSH and SO coil design. Targets from left to right: prefrontal cortex, temporal lobes (bilateral) and temporal lobe (unilateral).

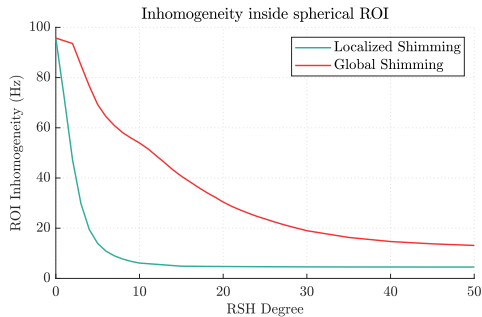




(a)



(b)



(c)

**Fig. 5:** Inhomogeneity assessment after shimming in four spherical ROIs, with ROIs 3 and 4 non-enclosing magnetic field sources, and ROIs 1 and 2 virtually enclosing such sources. Inhomogeneity as RSH degree increases (a) and fieldmap in a sagittal slice after 50<sup>th</sup> degree shimming (b) are shown. Inhomogeneity evolution inside ROI 4 is also compared under localized and global shimming (c).

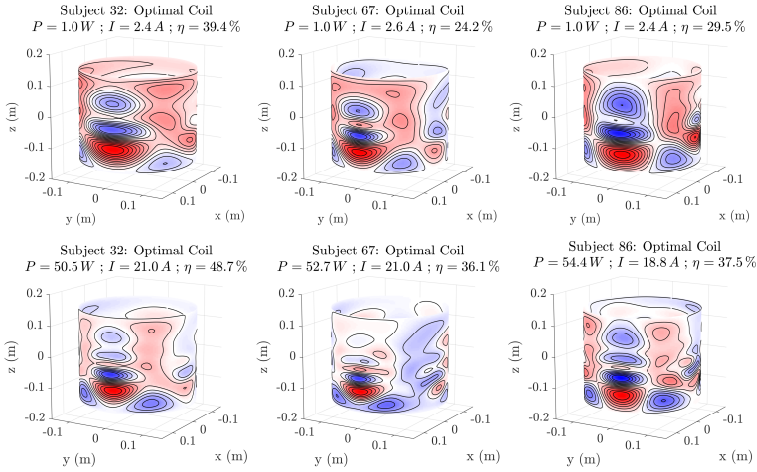


**Fig. 6:** Wire geometric centers of subject-optimal coils for 3 subjects at two different performances and power dissipation for each subject. The colormap represent the Stream Function intensity around the cylindrical surface (red is positive, blue is negative, which gives the sign of the current flow in the depicted windings)[13].

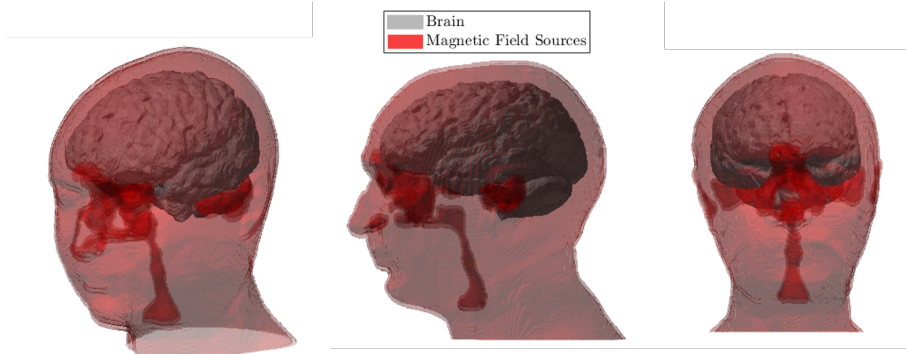
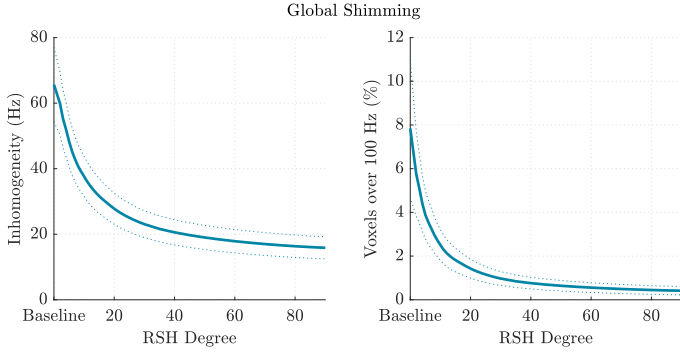
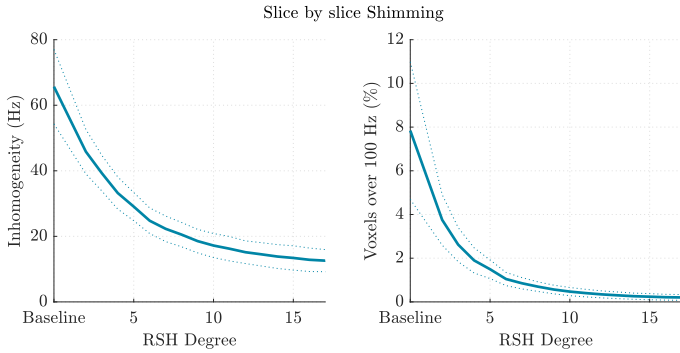


**Fig. 7:** Magnetic field source disposition around the human brain as computed from equation 2. The deep red color is representative of a large susceptibility laplacian coming from the difference between air and tissue susceptibilities, typically an order-of-magnitude above the inner tissue disparities, associated voxels are those in contact with air in head cavities (inner ear canals, sinus. . .). Amongst them, those close to or in contact with the brain contribute to the main  $B_0$ -field inhomogeneities therein.



(a)



(b)

**Fig. 8:** Average inhomogeneity and proportion of voxels over 100 Hz across subjects in the database as RSH degree increases (reference field at 7 T). Metrics for each subject are computed considering all voxels in the brain mask after application of (a) global and (b) slice by slice shimming. Dotted lines indicate standard deviation of the metric across subjects in the database.

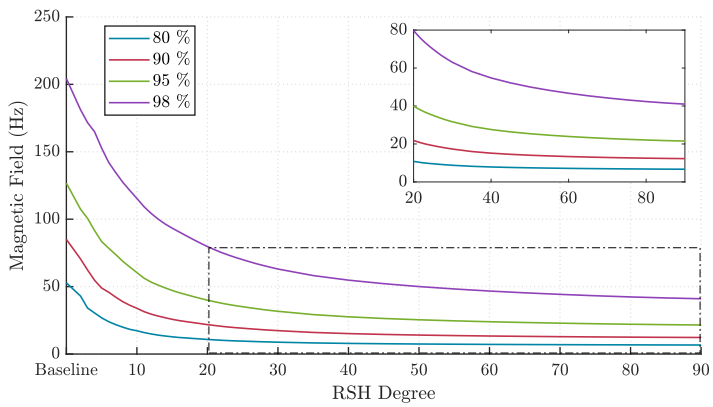


**Fig. 9:** 100-subject database average of the absolute frequency range containing 80 , 90 , 95 and 98 % of voxels in the brain after global shimming as RSH degree increases.

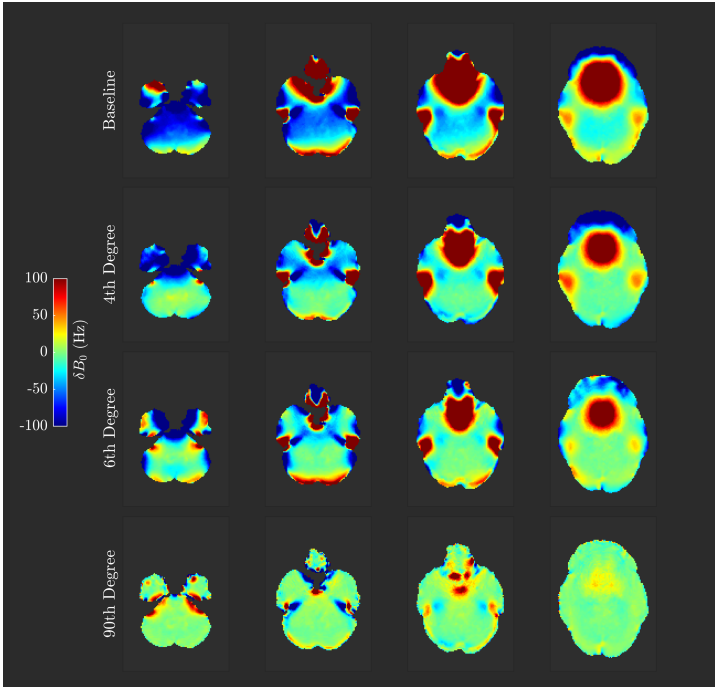
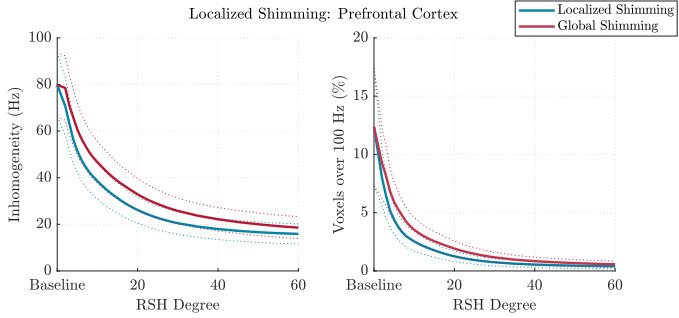
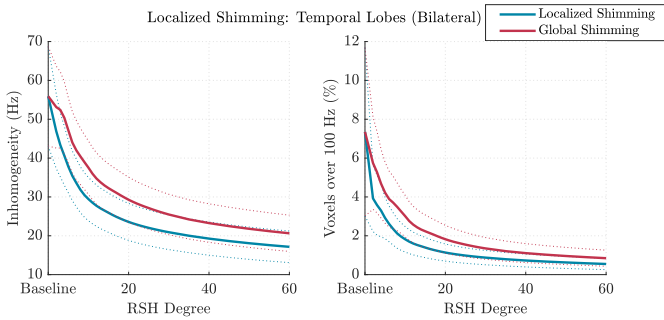


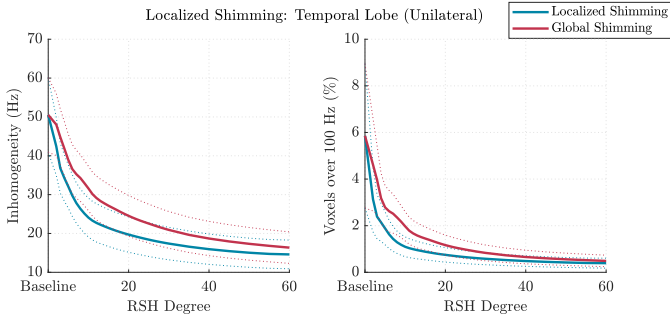
**Fig. 10:** Selected axial slices of brain fieldmap after RSH global shimming of different degrees. The slices show zones of high inhomogeneity. 4<sup>th</sup> and 6<sup>th</sup> degree fieldmaps are shown as examples of the maximum mitigation levels achieved by shimming systems so far as reported in the literature when performing global shimming. The best inhomogeneity obtained (90<sup>th</sup> degree shimming) in our unconstrained simulations is also shown.



(a)

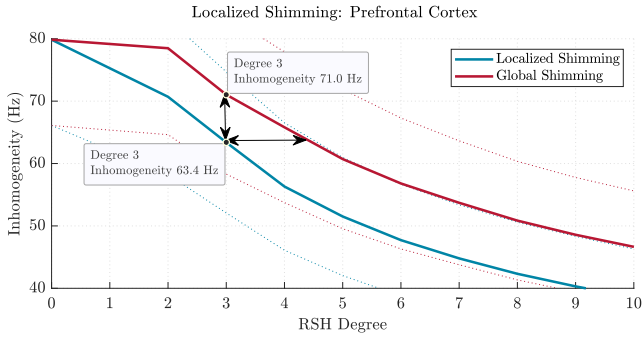


(b)

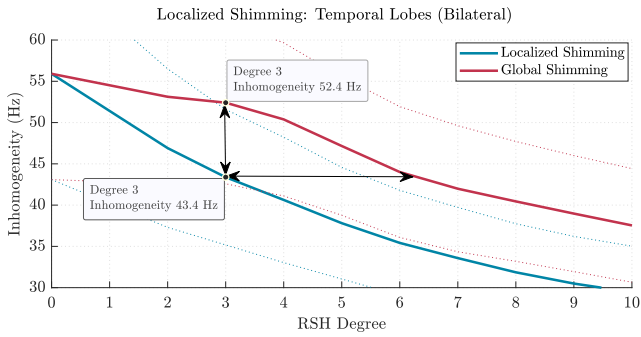


(c)

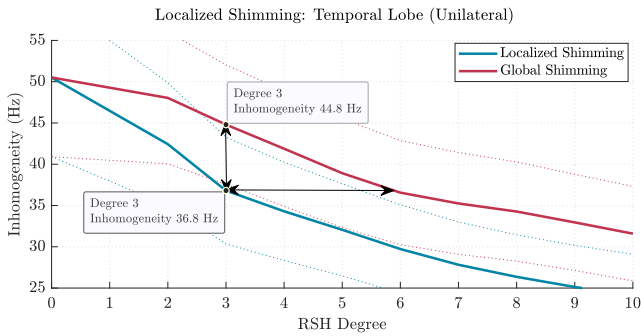
**Fig. 11:** Average inhomogeneity and proportion of voxels over 100 Hz across subjects in the database after global and localized RSH shimming of increasing degree. Metrics for each subject are computed considering the voxels inside target slabs enclosing the: (a) prefrontal cortex, (b) both temporal lobes and (c) a single temporal lobe. Dotted lines indicate standard deviation of the metric across subjects in the database.



(a)

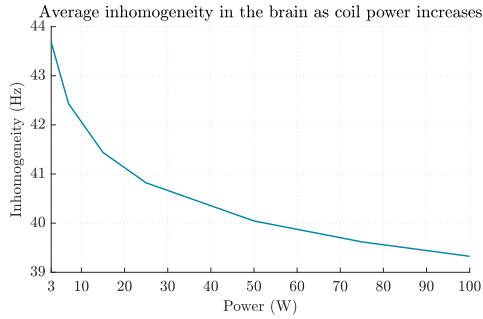


(b)

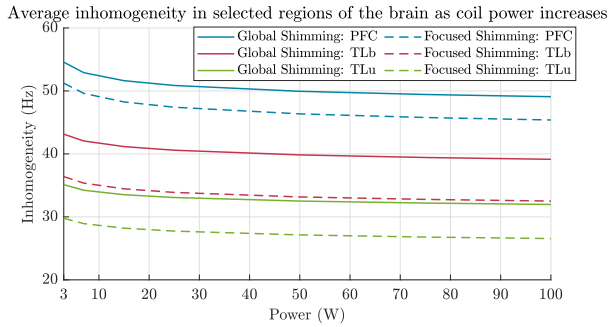


(c)

**Fig. 12:** Zoomed depiction of average inhomogeneity across the database in selected slabs for performance comparison between global and localized shimming techniques.



(a)



(b)

**Fig. 13:** Average inhomogeneity across fieldmaps after subject-optimal coil shimming when designed for (a) global shimming and (b) region-optimized shimming. In (b), dotted lines represent the inhomogeneity obtained with region-specific coils and the solid line represents the inhomogeneity within a specific region after whole-brain shimming optimized coils.